Direct Silicon Heterostructures With Methylammonium Lead Iodide Perovskite for Photovoltaic Applications

Silvia Mariotti, Mohammed Al Turkestani, Oliver S. Hutter, Georgios Papageorgiou, Jonathan D. Major, Jack Swallow, Pabitra K. Nayak, Henry J. Snaith, Vinod R. Dhanak, and Ken Durose

***Abstract*—We investigated the formation of photovoltaic (PV) devices using direct n-Si/MAPI (methylammonium lead tri-iodide) two-sided heterojunctions for the first time (as a possible alternative to two-terminal tandem devices) in which charge might be generated and collected from both the Si and MAPI. Test structures were used to establish that the n-Si/MAPI junction was photoactive and that spiro-OMeTAD acted as a "pinhole blocking" layer in n-Si/MAPI devices. Two-terminal "substrate" geometry devices comprising Al/n-Si/MAPI/spiro-OMeTAD/Au were fabricated and the effects of changing the thickness of the semitransparent gold electrode and the silicon resistivity were investigated. External quantum efficiency and capacitance–voltage measurements determined that the junction was one-sided in the silicon—and that the majority of the photocurrent was generated in the silicon, with there being a sharp cutoff in photoresponse above the MAPI bandgap. Construction of band diagrams indicated the presence of an upward valence band spike of up to 0.5 eV at the n-Si/MAPI interface that could impede carrier flow. Evidence for hole accumulation at this feature was seen in both Kelvin-probe transients and from unusual features in both current–voltage and capacitance–voltage measurements. The devices achieved a hysteresis-free best power conversion efficiency of 2.08%, V_{OC} 0.46 V, J_{SC} 11.77 mA/cm^2, and FF 38.4%, demonstrating for the first time that it is possible to create a heterojunction PV device directly between the MAPI and n-Si. Further prospects for two-sided n-Si/MAPI heterojunctions are also discussed.**

***Index Terms*—Heterojunctions, heterostructures, MAPI/silicon methylammonium lead iodide, methylammonium lead tri-iodide (MAPI), silicon.**

I. Introduction

THE hybrid organic–inorganic perovskite material methylammonium lead tri-iodide (MAPI) and its analogs have rapidly established themselves as important candidates for photovoltaic (PV) applications. While the PV performance of single-junction n-i-p devices has reached impressive levels (power conversion efficiency—PCE) of 25.2% [1], it is likely that perovskite materials will find their first commercial applications in tandem solar cells with silicon. MAPI's bandgap of 1.6 eV makes it a potentially ideal top junction partner for silicon, which has the lower bandgap of 1.1 eV. Recently a two-junction two-terminal tandem solar cell of this type using a MAPI analog has achieved a PCE of 28% [1], [2].

In this article, we investigated a different approach in which we formed direct heterojunctions between the MAPI and wafer n-Si. The eventual goal of this approach is to form a two-terminal heterojunction solar cell in which both sides of the heterojunction contribute to photocurrent generation and harvesting. Such a structure would have the advantage over a two-terminal tandem device of having a simple structure without the need for tunnel junctions connecting the two diodes in a tandem architecture. Previous attempts to make organic/silicon heterostructures include junctions with conducting polymers for PV include poly(3,4-ethylenedioxythiophene):poly(styrenesulfonate) (PEDOT:PSS) and poly (3-hexylthiophene) (P3HT) [3]–[6]. For the devices of this type, that from Zielke *et al.* [7] using Si/PEDOT:PSS have achieved the highest PCE at 20.6%.

In order to design and to understand the behavior of PV devices containing MAPI/n-Si junctions, it was necessary to first determine the junction type (i.e., ohmic or rectifying) of all the interfaces that are present in the device. In some cases, these are reported in the literature. For example, Au/MAPI [8], Au/spiro-OMeTAD, and Al/n-Si [9] are all ohmic, while Au/n-Si is known to be rectifying [10]. However, the authors found no papers that characterize the junction behavior of the widely deployed combination MAPI/spiro-OMeTAD, or the

Manuscript received December 18, 2019; revised February 27, 2020; accepted March 8, 2020. Date of publication April 20, 2020; date of current version June 19, 2020. This work was supported by the Engineering and Physical Sciences Research Council Centre for Doctoral Training in New and Sustainable Photovoltaics CDT-PV under Grant EP/L01551X/1. *(Corresponding author: Silvia Mariotti.)*

Silvia Mariotti was with the Stephenson Institute for Renewable Energy, Department of Physics, University of Liverpool, L69 7ZF Liverpool, U.K. She is now at University of Bordeaux (Laboratoire de Chimie des Polymères Organiques, LCPO UMR 5629 CNRS, Université de Bordeaux INP), F-33615 Pessac, Cedex, France (e-mail: silvia.mariotti@u-bordeaux.fr).

Mohammed Al Turkestani is with the Department of Physics, Umm Al-Qura University, Makkah 21955, Saudi Arabia (e-mail: mkturkestani@uqu.edu.sa).

Oliver S. Hutter, Jonathan D. Major, Jack Swallow, Vinod R. Dhanak, and Ken Durose are with the Department of Physics, Stephenson Institute for Renewable Energy, University of Liverpool, L69 7ZF Liverpool, U.K. (e-mail: o.s.hutter@liverpool.ac.uk; jonmajor@liverpool.ac.uk; sgjswall@liverpool.ac.uk; v.r.dhanak@liverpool.ac.uk; ken.durose@liverpool.ac.uk).

Georgios Papageorgiou was with the Stephenson Institute for Renewable Energy, Department of Physics, University of Liverpool, Liverpool L69 7ZF, U.K. He is now with CTF Solar, 01109 Dresden, Germany (e-mail: georgios.papageorgiou@ctf-solar.com).

Pabitra K. Nayak and Henry J. Snaith are with the Department of Physics, Clarendon Laboratory, University of Oxford, OX1 2JD Oxford, U.K. (e-mail: pabitra.nayak@physics.ox.ac.uk; henry.snaith@physics.ox.ac.uk).

Color versions of one or more of the figures in this article are available online at http://ieeexplore.ieee.org.

Digital Object Identifier 10.1109/JPHOTOV.2020.2981805

This work is licensed under a Creative Commons Attribution 4.0 License. For more information, see https://creativecommons.org/licenses/by/4.0/

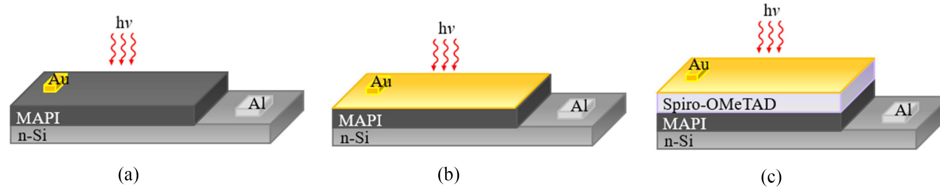

Fig. 1. Evolution of the wafer-based n-Si/MAPI superstrate device structure. (a) and (b) Device comprising Al/n-Si/MAPI/Au, in which the front contact pad is a 50-nm-thick gold dot and where this is combined with a larger area semitransparent (10 nm) gold film. (c) Al/n-Si/MAPI/spiro-OMeTAD/Au device, which uses the same combined gold contact pad and semitransparent gold electrode.

TABLE I
STUDY OF THE *J–V* AND EQE BEHAVIOR OF INTERFACES PRESENT IN Al/n-Si/MAPI/Au AND Al/n-Si/MAPI/spiro-OMeTAD/Au DEVICES, INCLUDING INTERFACES, SUCH AS n-Si/Au AND n-Si/spiro-OMeTAD THAT COULD FORM ACCIDENTALLY

Interface	Reference or structure tested in this work	J-V	EQE
n-Si/Al	[9]	Ohmic	N/A
MAPI/Au	[8]	Ohmic	N/A
Spiro-OMeTAD/Au	[8]	Ohmic	N/A
n-Si/Au	[10] Al/n-Si/Au	Rectifying: Schottky junction solar collector. AM1.5 average PCE 1.2%, V_{OC} 0.27 V, J_{SC} 13.6 mA/cm^2	Photocurrent generated above the absorption region of silicon
n-Si/MAPI	Al/n-Si/MAPI/Au	Rectifying: in light average PCE 0.1%, V_{OC} 0.30 V, J_{SC} 1.1 mA/cm^2. NB : the MAPI had pinholes	Current too low to be measured
n-Si/spiro-OMeTAD	Al/n-Si/spiro-OMeTAD/Au	Rectifying but only very weakly photo-active	N/A
MAPI/spiro-OMeTAD	Glass/Au/MAPI/spiro-OMeTAD/Au	Rectifying but not photo-active	N/A

junctions between the n-Si and either MAPI or spiro-OMeTAD. We also considered junctions that could form accidentally via electrical shunt paths in a PV device based on the n-Si/MAPI heterojunctions, including n-Si/spiro-OMeTAD and n-Si/Au.

The most viable design we tested was a "superstrate" type device having the structure Al/n-Si/MAPI/spiro-OMeTAD/Au, which we investigated with regard to the thickness of semitransparent gold and the silicon doping density. This device achieved a hysteresis-free best PCE of 2.08%, V_{OC} 0.46 V, J_{SC} 11.77 mA/cm^2, and FF 38.4%, demonstrating for the first time that it is possible to create a photoactive heterojunction PV device directly between the MAPI and n-Si.

II. EXPERIMENTAL METHOD

Devices having the "substrate" configuration and having two different structures were fabricated on silicon wafers and tested using the procedures and layer orders described in the following. These were Al/n-Si/MAPI/Au and Al/n-Si/MAPI/spiro-OMeTAD/Au. For Al/n-Si/MAPI/Au, two variants were fabricated, as shown in Fig 1(a) and (b). In the first, 50-nm-thick gold dots measuring 1 × 5 mm^2 were applied to the illuminated (top) surface of the MAPI. In the second, a larger area semitransparent gold contact (3 × 5 mm^2 and 10 nm thick) was also applied in order to increase lateral conductivity. For Al/n-Si/MAPI/spiro-OMeTAD/Au, the dual thickness front-side gold contact (as above) was used throughout. The performance of the devices was measured as a function of the semitransparent gold thickness in the range 5–20 nm and, also, as a function of the silicon resistivity (see Fig. 1).

In addition, test structures designed to determine the ohmic or rectifying nature of the combinations of materials that could occur in these devices were also fabricated. These made the use of known ohmic combinations from the literature, including Au/MAPI and Au/spiro-OMeTAD. Details of the test structures themselves may be found in Table I. Where the junction under test was a combination of an organic material and silicon, then known ohmic contacts could be applied to both components directly. For cases where contacts to an organic were to be tested, then the organic was spin-coated so as to partly cover a metallic film on the glass. This enabled a top contact of a different metal to be applied while allowing both sides of the film to be accessed by electrical probes for measurement. Junction combinations tested here include n-Si/MAPI, n-Si/ spiro-OMeTAD and MAPI/ spiro-OMeTAD.

Batches of (001) oriented n-type (phosphorous doped) silicon wafers having resistivities in the ranges 1–5 Ω·cm ($n = 0.9$–4.8×10^{15} cm^{-3}), 5–10 Ω·cm ($n = 4.4$–9.0×10^{14} cm^{-3}), and 10–15 Ω·cm ($n = 2.9$–4.4×10^{14} cm^{-3}) obtained from Pi-KEM, Ltd., were used in device fabrication, while a batch having resistivities in the range 1—10 Ω·cm was used for preliminary experiments. Prior to spin coating, the wafers were cleaned using the RCA procedure (see [11]), which involves finishing using HF etching to remove the native oxide.

MAPI films were deposited using a single-step spin-coating process in a glovebox. The precursor solution was prepared by dissolving lead iodide (PbI_2) and methylammonium triiodide (CH_3NH_3I) in N,N-dimethylformamide/dimethyl sulfoxide. The layers were then annealed at 100 °C to form MAPI layers 400–450 nm thick.

Films of doped spiro-OMeTAD (2,2',7,7'-Tetrakis[N,N-di(4-methoxyphenyl)amino]-9,9'-spirobifluorene) were spin-coated from solution in chlorobenzene.

Gold and aluminum used for contacting were thermally evaporated with the thicknesses being monitored using a quartz thickness monitor.

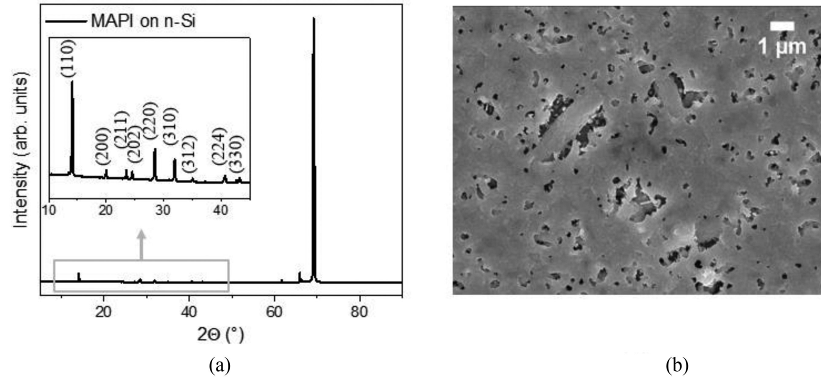

Fig. 2. Characterization of spin-coated MAPI layers on an n-type silicon wafer. (a) XRD analysis showing peaks corresponding to the tetragonal structure of the perovskite (main peaks for (110), (220), (310), and (330) at 14.1°, 28.5°, 31.9°, and 43°, respectively). (b) SEM image showing the MAPI surface with numerous large voids.

Current–voltage characteristics of the junctions tested were measured using a Kiethley 2400 source meter. Solar cell J–V measurements were conducted under approximate AM1.5 conditions at 1000 W.m^{-2} using a TS Space Systems solar simulator. External quantum efficiency spectra were measured using a Bentham PVE300 system with white light bias. Capacitance–voltage data were measured at 10^5 Hz using a Solartron 1260 frequency response analyzer with a 1296 dielectric interface. MAPI films were evaluated by θ-2θ X-ray diffraction (XRD) using a Philips X'pert system and by scanning electron microscopy (SEM) using a JEOL 7001 instrument. Optical transmission spectra were recorded using a Shimadzu UV3600 UV-Vis-IR spectrophotometer. X-ray photoelectron (XPS) spectra were measured using an Al Kα source (1486.7 eV) in an in-house built spectrometer having a resolution of 0.4 eV. Kelvin-probe measurement of work functions was done at the University of Oxford and was referenced to freshly cleaved highly ordered pyrolytic graphite.

III. Results and Discussion

A. *Deposition and Qualification of Methylammonium Lead Tri-Iodide Films on Silicon (001)*

The crystallinity and morphology of MAPI on Si (001) was determined by XRD and SEM, as shown in Fig. 2(a) and (b). The most intense XRD peak in Fig. 2(a) is at $2\theta = 69.2°$, which corresponds to the Si (001) peak [12]. The inset in the figure shows the region $10 > 2\theta > 50°$ that contains MAPI's main peaks and confirms that spin coating has successfully formed polycrystalline MAPI films on silicon wafers. The SEM image in Fig. 2(b) shows that although the spin coating of MAPI achieved full coverage of the silicon wafer, there were numerous pinholes and voids. This finding indicates that if such films are incorporated into a multilayer device, there is the possibility of shunting through the MAPI.

Further characterization of the MAPI was performed on identical samples deposited on glass. UV-Vis-IR spectroscopy determined the bandgap to be $E_g = 1.57$ eV. XPS estimation of the Fermi level position as being 0.87 eV above the valence, therefore, indicated the MAPI to be intrinsic.

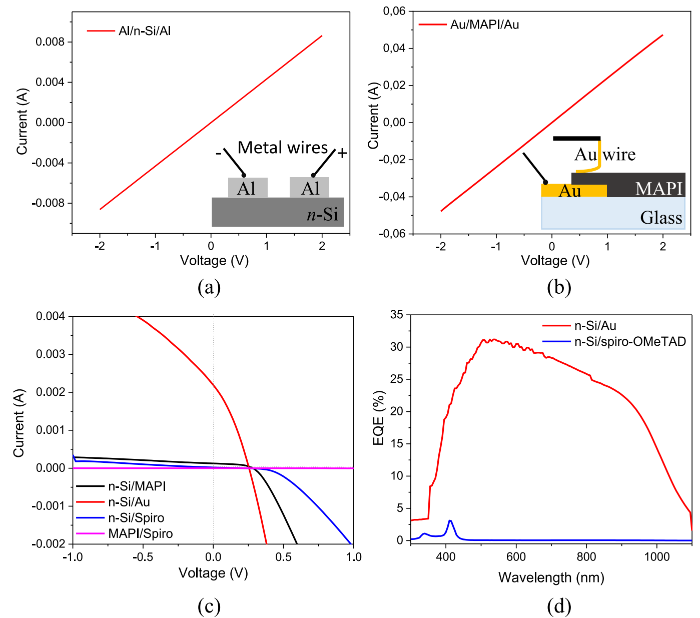

Fig. 3. I–V and EQE (where applicable) measurements of the device's interfaces that are present or may form in the device because of shunting. I–V measurement on (a) n-Si/Al and (b) MAPI/Au contacts, proving their ohmic behavior. (c) Forward I–V scans under AM1.5 illumination of the rectifying combinations. (d) EQE measurement on n-Si/spiro-OMeTAD and n-Si/Au.

B. *Junction Properties of Material Combinations for Use in n-Si/MAPI Devices*

In this section, we report the use of light J–V curves and EQE spectroscopy to determine the ohmic or rectifying nature of the various combinations of materials that may occur in n-Si/MAPI devices.

The ohmic behaviors of n-Si/Al and Au/MAPI are shown in Fig. 3(a) and (b), respectively. Although Al is not an ideal metal for contacting n-Si because of the high resistance (slope $= 1/R$, $R = 231\ \Omega$), this was used as an ohmic contact [see Fig. 3(a)]. Resistance calculated from the I–V curve between the Au and MAPI was calculated as $42\ \Omega$ [see Fig. 3(b)]. The ohmic behavior of Au/spiro-OMeTAD is reported in the literature and, hence, it is not discussed further here.

Both the *J–V* and EQE results for 1) MAPI/spiro-OMeTAD, 2) n-Si/spiro-OMeTAD, 3) n-Si/MAPI, and 4) n-Si/Au are shown in Fig. 3(c) and (d) and summarized in Table I.

1) For MAPI/spiro-OMeTAD, the light *J–V* for this structure showed a straight line and no photoactivity that indicates the junction is ohmic. (We used ohmic gold contacts to both the MAPI and spiro-OMeTAD, which were deposited on glass substrates.)
2) For the case of n-Si/spiro-OMeTAD, the junction was rectifying but only very weakly photoactive, showing only a small peak in the EQE spectrum corresponding to the near bandgap energy of spiro-OMeTAD at 3 eV or 413 nm.
3) For the combination of n-Si/MAPI, the junction showed rectification but only weak photoactivity (PCE of just 0.1%), making it impossible to record an EQE spectrum. Nevertheless, this junction was developed later in this work into fully operating PV devices.
4) Finally, n-Si/Au formed a photoactive Schottky junction solar cell, as may be seen from the *J–V* and EQE responses in Fig. 3(c) and (d). The photoresponse is relatively strong, with the EQE having an onset for above-gap wavelengths in the silicon and persisting until below 400 nm. This junction would not form an intentional part of our solar cell designs, but in principle, it could form accidentally if there were shunting paths through the active organic layers.

These results have implications for the formation of devices. First, the MAPI/spiro-OMeTAD junction is rectifying but not photoactive and is, therefore, not expected to make any direct contribution to the photocurrent in any devices. Second, we consider the effect of the pinholes in MAPI absorbers deposited on silicon substrates, as shown in Fig. 2. If a direct Au contact is used on MAPI with pinholes, then it is possible that an n-Si/Au junction will form accidentally, and that it will have its own photoresponse. On the other hand, if spiro-OMeTAD is deposited on the top of MAPI, then any accidental contact between the n-Si and spiro-OMeTAD is not expected to be consequential. In fact, spiro-OMeTAD might be expected to be a "pinhole blocker" as is discussed later [13]. These inferences were tested in the fabrication of devices, as reported in Section III-C.

C. Initial Device Results and Evolution of the Device Structure

Devices having all the structures shown in Fig. 1(a)–(c) were fabricated and tested. Initially, Al/n-Si/MAPI/Au devices with gold dot top contacts [see Fig. 1(a)] were fabricated, but these yielded no photocurrent since there was no lateral conductor on the illuminated surface. Hence the structure in Fig. 1(b) was adopted, with the top electrode comprising an ultrathin semitransparent gold film. This structure was weakly photoactive, giving a PCE of 0.13% (V_{OC} = 0.30 V, J_{SC} = 1.12 mA/cm^2, FF = 37.7%). Since it was suspected that the pinholes in the MAPI [see Fig. 2(b)] were causing shunting, a film of spiro-OMeTAD was added to the MAPI to give the structure, as shown in Fig. 1(c), the full structure now being Al/n-Si/MAPI/spiro-OMeTAD/Au. Fig. 4(a) shows the SEM cross section of the device structure. Current–voltage curves of both types of devices are compared in Fig. 4(b), which shows that all the working parameters of the devices (V_{oc}, J_{sc}, and FF) were increased by the inclusion of the spiro-OMeTAD.

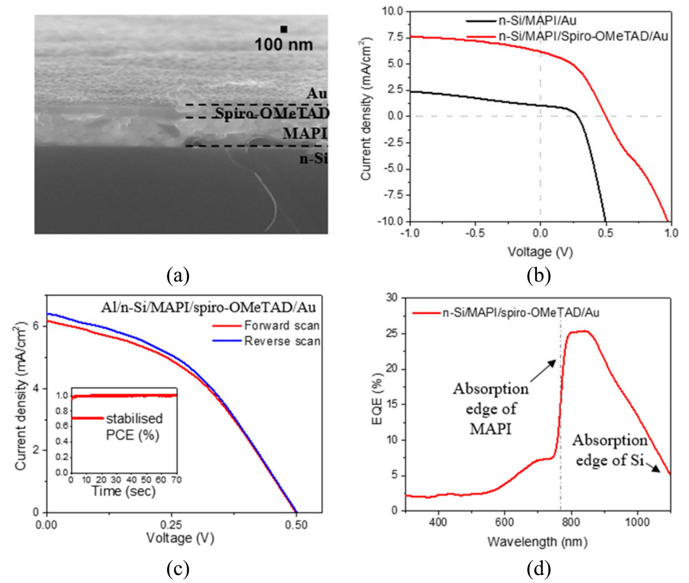

Fig. 4. Device characterization. (a) Cross-sectional SEM of an Al/n-Si/MAPI/spiro-OMeTAD/Au device, showing a perovskite layer with a thickness of 400 nm. (b) *J–V* measurement under AM1.5 illumination comparing Al/n-Si/MAPI/Au and Al/n-Si/MAPI/spiro-OMeTAD/Au devices, where the device containing the hole-transporting material shows an increased current density and open circuit voltage. (c) *J–V* data present both forward and reverse scans to show the hysteresis-free behavior of these heterojunctions. An inset with the stabilised efficiency graph is added for the highest performing device and shows high stability. (d) EQE analysis on Al/n-Si/MAPI/spiro-OMeTAD/Au device showing strong collection in the silicon but a step change downward above the bandgap of MAPI at 750 nm.

TABLE II
Al/*n*-Si/MAPI/spiro-OMeTAD/Au Average Device Performances Measured Under AM1.5 Illumination, With Standard Deviation in Brackets (N = 10 for Each Thickness)

Au thickness (nm)	PCE (%)	V_{OC} (V)	J_{SC} (mA/cm^2)	FF (%)
0	0.10 (± 0.07)	0.36 (± 0.02)	1.02 (± 0.46)	24.7 (± 6.3)
5	0.13 (± 0.05)	0.43 (± 0.02)	0.88 (± 0.26)	32.6 (± 4.1)
10	1.14 (± 0.12)	0.49 (± 0.01)	5.56 (± 0.48)	41.8 (± 0.7)
15	0.92 (± 0.12)	0.48 (± 0.01)	5.35 (± 0.51)	35.6 (± 1.5)
20	0.92 (± 0.12)	0.48 (± 0.01)	5.24 (± 0.79)	36.6 (± 2.5)

Top contact comprises a small gold pad for probing (50-nm thick), with a larger semitransparent gold electrode having a thickness in the range 1–20 nm.

Since spiro-OMeTAD does not form a low-resistance contact with n-Si, any accidental contact between the spiro-OMeTAD and n-Si through pinholes in the MAPI is not expected to give shunt loss. Instead, spiro-OMeTAD is likely to act not only as a contact material for the MAPI but also as a pinhole blocking layer. Similar pinhole blocking has been reported before for other spin-coated organic films used in contacting PV devices [13], [14].

The effect of varying the thickness of the semitransparent gold contact on the n-Si/MAPI/spiro-OMeTAD/Au device performance is listed in Table II. In addition of this, electrode causes a step up in performance when the gold reaches 10 nm thickness, giving an increase in the short-circuit current from

TABLE III
RESULTS FROM *C–V* ANALYSIS PERFORMED ON Al/n-Si/MAPI/spiro-OMeTAD/Au DEVICES USING Si WAFERS HAVING DIFFERENT RESISTIVITIES AND USING THE SINGLE-SIDED JUNCTION APPROXIMATION

Si resistivity / AVG carrier concentration	V_{bi} (V)	PCE (%)	V_{OC} (V)	J_{SC} (mA/cm^2)	FF (%)
1-5 Ω·cm /	Average	1.26 (± 0.64)	0.42 (± 0.05)	7.26 (± 5.28)	46.2 (± 9.8)
2.86 x 10^{15} cm^{-3}	Best	2.08	0.46	11.77	38.4
5-10 Ω·cm /	Average	1.08 (± 0.56)	0.43 (± 0.06)	6.20 (± 2.77)	37.8 (± 9.5)
6.68 x 10^{14} cm^{-3}	Best	2.07	0.48	13.92	30.9
10-15 Ω·cm /	Average	1.02 (± 0.22)	0.41 (± 0.04)	6.45 (± 1.86)	39.70 (± 7.14)
3.67 x 10^{14} cm^{-3}	Best	1.34	0.46	6.22	46.7

Vbi decreases slightly with increasing N-Si resistivity, while the carrier concentrations for the N-Si measured from Mott-Schottky plots from the devices is a close match to those of the wafers used.

about 1 to 5 mA·cm^{-2}. Devices having 10-nm-thick electrodes had marginally higher performance than for greater gold thicknesses with the average ($N = 10$) PCE being 1.14% ($V_{OC} = 0.46$ V, $J_{SC} = 5.56$ mA/cm^2, and FF $= 41.8\%$) and the highest device efficiency being 1.35%, with $V_{OC} = 0.50$ V, $J_{SC} = 6.42$ mA/cm^2, and FF $= 42.0\%$.

Fig. 4(c) shows both the forward and reverse *J–V* curves for a Al/n-Si/MAPI/spiro-OMeTAD/Au device (scan rate 0.19 V·s^{-1}) as well as the "stabilized efficiency" as a function of time during the initial period when the greatest changes are expected. The *J–V* responses show very little hysteresis compared with some conventional MAPI device structures [15]. Moreover, the efficiency does not vary greatly with time, and in particular, there is no initial rapid drop off in efficiency as is seen for MAPI devices [16]. These stability indicators are encouraging for future n-Si/MAPI devices.

An external quantum efficiency spectrum for a typical device from this series is shown in Fig. 4(d). At long wavelengths, the response from the silicon dominates, with there being a gradual EQE onset at the silicon bandgap energy of 1.1 eV (∼1100 nm). However, at around 750 nm, corresponding to the bandgap of MAPI (1.57 eV), there is a sharp drop in EQE level from about 25% at its peak down to about 7%. For shorter wavelengths, the EQE remains low but nonzero (2%–7%). The spectrum may be interpreted as implying that absorption in the silicon contributes to the photocurrent, but that photoexcited carriers in the MAPI do not contribute, or else only contribute weakly, to the photocurrent. In these devices at least, MAPI appears to be acting as a parasitic absorber. Indeed, similar EQE responses have been reported for tandem silicon-MAPI devices in which absorption loss in the MAPI top junction leaves a similar deficit in the EQE spectrum of the underlying silicon. In the present case of a direct homojunction, this could be a result of the electrical junction between the MAPI and the n-Si being one sided, i.e., there is an electric field present in the silicon, which is capable of harvesting photoexcited carriers but not in the MAPI. Hence, in Section III-D, we report on the behavior of devices made with silicon having different doping densities since this could change the position of the junction and, hence, photoresponse.

D. Devices With Silicon Having Different Resistivities

In order to establish the effect of the n-Si wafer on the PV performance of the n-Si/MAPI heterojunction, a series of devices having the same structure, as above (Al/n-Si/MAPI/spiro-OMeTAD/Au), were fabricated on wafers having different resistivities and carrier concentrations. These were 1–5, 5–10, and 10–15 Ω·cm corresponding to the doping densities of 0.9–4.8 × 10^{15} cm^{-3}, 4.4–9.0 × 10^{14} cm^{-3}, and 2.9–4.4 × 10^{14} cm^{-3}, respectively. The average and best device parameters from the sets of ten devices are listed in Table III, while typical *J–V*, EQE, and *C–V* data are shown in Fig. 5. The average efficiencies, V_{oc}, J_{sc}, and FF values are all similar within experimental error, but there is nevertheless a trend for the highest performing devices from each batch. The highest efficiencies were obtained for the lowest resistivity substrates with PCE = 2.08%, V_{OC} 0.46 V, J_{SC} 11.77 mA/cm^2, and FF 38.4%. Devices made on the higher resistivity material show a slight decline in efficiency, as shown in Fig. 5(a). The EQE of best devices [see Fig. 5(b)] shows the same trend as the efficiencies and shows the same absorption edge behavior as described above, i.e., with

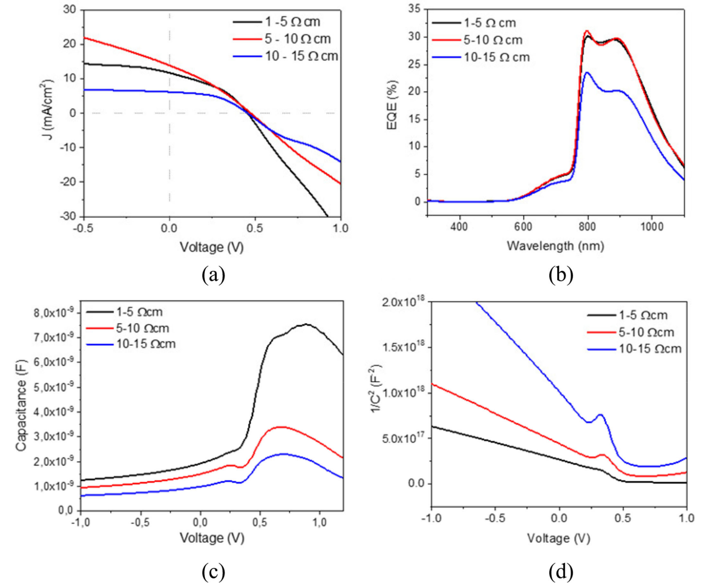

Fig. 5. Characterization of Al/n-Si/MAPI/spiro-OMeTAD/Au devices having different silicon resistivities. (a) Best *J–V* curves of devices for each silicon doping concentration. (b) EQE spectra showing absorption edges, which behave independently to the silicon's resistivity. (c) *C–V* characterization showing two main peaks: A smaller at $V \sim 0.25$ V and a more intense capacitance peak at $V > 0.5$ V. (d) Mott-Schottky plot deriving from *C–V* measurement. The fitting of the curves provides similar V_{bi} in the range of 0.65–0.70 V for devices made with different doping concentrations of the silicon.

TABLE IV
RESULTS FROM C–V ANALYSIS PERFORMED ON Al/n-Si/MAPI/spiro-OMeTAD/Au DEVICES USING SI WAFERS HAVING DIFFERENT RESISTIVITIES AND USING THE SINGLE-SIDED JUNCTION APPROXIMATION

Si resistivity	V_{bi} (V)	Manufacturer's n-Si carrier concentration (cm^{-3})	C-V n-Si carrier concentration (cm^{-3})
1-5 Ω·cm	0.70 ± 0.01	2.86 x 10^{15}	1.39 x 10^{15}
5-10 Ω·cm	0.68 ± 0.01	6.68 x 10^{14}	7.90 x 10^{14}
10-15 Ω·cm	0.65 ± 0.01	3.67 x 10^{14}	3.28 x 10^{14}

$V_{\rm bi}$ decreases slightly with increasing n-Si resistivity, while the carrier concentrations for the n-Si measured from Mott-Schottky plots from the devices is a close match to those of the wafers used.

the EQE being reduced stepwise above the absorption threshold for MAPI.

C–V measurements and the corresponding Mott-Schottky plots ($1/C^2$–V) are shown in Fig. 5(c) and (d). For all devices, the C–V data show a main peak at > 0.5 V and an unusual smaller discontinuity at about 0.25–0.3 V that is more clearly visible in the $1/C^2$–V plots as a peak. This decreases in magnitude with increasing doping density in the silicon and may be related to an interface barrier effect that is discussed later.

Table IV lists the built-in voltage ($V_{\rm bi}$) [17] and carrier concentration values extracted from the $1/C^2$–V plots. The built-in voltages for all devices were in the range 0.65–0.70 V. Since these are somewhat greater than the $V_{\rm oc}$ values obtained experimentally (0.41–0.43 V), there is clearly some room for improvement in practical devices. The carrier concentrations were extracted from the $1/C^2$–V plots using the one-sided junction approximation, which was justified from the EQE response, which is strong in the silicon absorption region but weaker in MAPI's. In all cases, the carrier concentration values extracted using the one-sided junction model from the devices were good match with the carrier concentrations for the n-Si wafers used. Hence, from both the EQE and the C–V evidence, it is most likely that the n-Si/MAPI junction is one-sided and lies in the n-Si.

Nevertheless, since the rationale for fabricating n-Si/MAPI heterojunctions was to enhance photon harvesting from both the sides of the junction, we have given some consideration to both the possibility of two-sided junctions as well as the cases where the band bending (field) lies entirely in the n-Si or in the MAPI. First, we applied the two-sided junction approximation to the C–V data, with the results for the apparent carrier concentrations. The outcome was that the carrier densities attributed to the MAPI were in the range $8 \times 10^{14} - 1 \times 10^{15}$ cm^{-3}. While these are at the higher end of the range of values reported for experiments on MAPI (10^9–10^{15} cm^{-3}) [18], their close correspondence with the concentration values extracted for the silicon and the asymmetric nature of the EQE curves make the two-sided junction analysis unconvincing. Hence, we restrict our further remarks to an evaluation of the band line ups for the n-Si/MAPI heterojunction for the cases of the junction being one sided in either the n-Si or the MAPI—and some corroborative data from Kelvin-probe measurements.

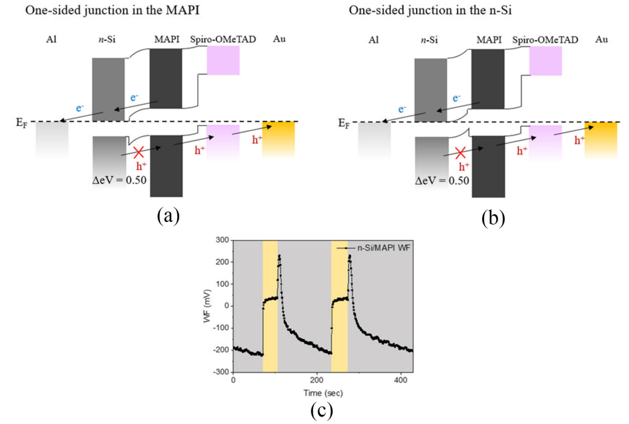

Fig. 6. Band alignments and Kelvin-probe analysis. (a) and (b) Equilibrium band diagrams for an Al/n-Si/MAPI/spiro-OMeTAD/Au device, constructed using the literature data [19], [20] for one-sided junctions. In (a), the field is presumed to be in the MAPI, whereas in (b), it is in the n-Si. Both have a valence band discontinuity that could block hole transport. (c) Kelvin-probe measurement obtained from an Al/n-Si/MAPI structure, showing the measured CPD versus time, with the yellow and gray shading that indicates light and dark conditions, respectively. The spike occurring after the light is switched OFF is presumed to be due to hole accumulation because of the valence band discontinuities (see text).

E. Band Diagrams and Evidence for a Valence Band Discontinuity Between n-Si and Methylammonium Lead Tri-Iodide

We constructed equilibrium band diagrams for the n-Si/MAPI junction having an Al contact to the n-Si and spiro-OMeTAD to the MAPI, as shown in Fig. 6. The band data were obtained from the literature [19], [20] and the fermi levels were positioned appropriately for the doping with the MAPI being intrinsic and the spiro-OMeTAD being p-type [21]. Here, we considered the two cases of one-sided junctions with the field being either in the MAPI [see Fig. 6(a)] or in the n-Si [see Fig. 6(b)]. Both show a valence band discontinuity of ∼0.5 eV between the n-Si and the MAPI. For the case of the field being in the MAPI, the spike points downward in the valence band at the MAPI/silicon interface [see Fig. 6(a)]. Hence, while both electrons and holes generated in the MAPI would drift unimpeded, photogenerated minority carrier holes in the (field free) n-Si would be blocked by the barrier. On the other hand, for the case of the band bending being in the n-Si [see Fig. 6(b)], photogenerated holes from the silicon would encounter an upward valence band spike that could cause charge accumulation. However, since for this case, the MAPI is field free, charge collection from it is less likely, even though there are no barriers to charge transport on the band diagrams.

Further evidence of a barrier to charge flow comes from the Kelvin-probe measurement of an Al/n-Si/MAPI structure, as shown in Fig. 6(c). The graph shows a contact potential difference (CPD) ≤ -200 mV in the dark, which increases to 250–260 mV when light is applied—this is consistent with the injection of both electrons and holes from illumination. However, the sample shows an anomalous behavior when the light is switched OFF. There is a sudden increase in work function, which then decays away with time. This behavior is consistent with hole accumulation between the n-Si and MAPI [see Fig. 6(b)], which

then decays as the excess carriers recombine. Other evidences for such a barrier are: the unusual kinks in *J–V* curves that occur for $V > 0.5$ V [see, for example, Fig. 4(b)]—this is considered to indicate interface charging in a number of different technologies [22], [23]; the unusual peak in the $1/C^2$–V curves [see Fig. 5(d)]; and finally, the general trend of the PCE increasing slightly for the more highly doped silicon is consistent with the spike in the band diagram in Fig. 6(b) becoming smaller as the fermi level in the silicon moves away from the conduction band edge.

IV. Conclusion

Direct heterojunction PV devices between the n-Si and MAPI have been fabricated and investigated for the first time. The deposition of MAPI on n-Si by spin coating was successful and n-Si/MAPI test structures were fabricated and were used to demonstrate that the n-Si/MAPI junction is both rectifying and photoactive. Similarly, spiro-OMeTAD was shown to form an ohmic and nonphotoactive junction with MAPI, making it a suitable contact material but also having the benefit of acting as a "pinhole blocking" layer in devices. The two-terminal "substrate" geometry Al/n-Si/MAPI/spiro-OMeTAD/Au device configuration was explored. Light entered through an ultrathin semitransparent gold electrode having an optimum thickness of 10 nm. This, in combination with low-resistivity silicon wafers, gave a PCE of 2.1% ($V_{OC} = 0.46\,\mathrm{V}$, $J_{SC} = 11.77\,\mathrm{mA/cm^2}$, FF = 38.4%), with $V_{\rm bi}$ being 0.65–0.7 V. EQE responses for these devices showed strong collection from the n-Si but having attenuated collection above the MAPI bandgap. This and the close agreement between the doping densities of the n-Si wafers with the carrier densities from Mott-Schottky plots indicated that the junction in these n-Si/MAPI devices is one-sided and lies in the silicon. Band diagrams constructed for such junctions indicate an upward spike in the valence band up to 0.5 eV at the n-Si/MAPI interface. This was corroborated by the observation of a charge-trapping related transient in light/dark Kelvin-probe measurements. Further evidence of charge accumulation came from unusual kinks in both the *J–V* and *C–V* data. This band discontinuity could also account for the relatively low efficiency of collection of photogenerated carriers from the silicon in this device.

Overall, we have demonstrated a direct n-Si/MAPI heterojunction device structure. However, it has achieved collection from the Si only rather than from both the Si and MAPI. Hence, further developments—for example, using more highly conductive silicon or the control of the doping in MAPI—will be required to achieve the goal of a true two-sided heterojunction capable of simultaneous photon harvesting from both silicon and MAPI.

Further Data

Supplementary research data including spectra, band diagrams and data may be found at DOI: https://doi.org/10.17638/datacat.liverpool.ac.uk/1049.

References

[1] "NREL—Best research-cell efficiency chart—Photovoltaic research." [Online]. Available: https://www.nrel.gov/pv/cell-efficiency.html. Accessed on: Jun. 10, 2019.
[2] "Perovskite world record | Oxford PV perovskite solar cell achieves 28% efficiency," 2018. [Online]. Available: https://www.oxfordpv.com/news/oxford-pv-perovskite-solar-cell-achieves-28-efficiency. Accessed on: Sep. 4, 2019.
[3] T.-G. Chen, B.-Y. Huang, E.-C. Chen, P. Yu, and H.-F. Meng, "Micro-textured conductive polymer/silicon heterojunction photovoltaic devices with high efficiency," *Appl. Phys. Lett.*, vol. 5, no. 3, pp. 033301–033307, Jul. 2012.
[4] F. Zhang, B. Sun, T. Song, X. Zhu, and S. Lee, "Air stable, efficient hybrid photovoltaic devices based on poly (3-hexylthiophene) and silicon nanostructures," *Chem. Mater.*, vol. 23, no. 8, pp. 2084–2090, Mar. 2011.
[5] S.-C. Shiu, J.-J. Chao, S.-C. Hung, C.-L. Yeh, and C.-F. Lin, "Morphology dependence of silicon nanowire/poly(3,4-ethylenedioxythiophene):poly(styrenesulfonate) heterojunction solar cells," *Chem. Mater.*, vol. 22, no. 10, pp. 3108–3113, May 2010.
[6] K. A. Nagamatsu, S. Avasthi, J. Jhaveri, and J. C. Sturm, "A 12% efficient silicon/PEDOT:PSS heterojunction solar cell fabricated at < 100°C," *IEEE J. Photovolt.*, vol. 4, no. 1, pp. 260–264, Jan. 2014.
[7] D. Zielke *et al.*, "Organic-silicon solar cells exceeding 20% efficiency," *Energy Procedia*, vol. 77, pp. 331–339, 2015.
[8] F. Behrouznejad, S. Shahbazi, N. Taghavinia, H.-P. Wu, and E. Wei-Guang Diau, "A study on utilizing different metals as the back contact of $CH_3NH_3PbI_3$ perovskite solar cells," *J. Mater. Chem. A*, vol. 4, no. 35, pp. 13488–13498, 2016.
[9] D. C. Northrop and D. C. Puddy, "Ohmic contacts between evaporated aluminium and n-type silicon," *Nucl. Instrum. Methods*, vol. 94, no. 3, pp. 557–559, Jul. 1971.
[10] D. Kahng, "Conduction properties of the Au-n-type—Si Schottky barrier," *Solid-State Electron.*, vol. 6, no. 3, pp. 281–295, May/Jun. 1963.
[11] W. Kern and J. Vossen, "Cleaning procedures for silicon wafers." [Online]. Available: https://www.inrf.uci.edu/wordpress/wp-content/uploads/sop-wet-silicon-solvent-clean.pdf. Accessed on: Mar. 30, 2020.
[12] M. Cheragizade *et al.*, "Synthesis and characterization of PbS mesostructures as an IR detector grown by hydrogen-assisted thermal evaporation," *Mater. Sci. Semicond. Process.*, vol. 26, pp. 704–709, Oct. 2014.
[13] J. D. Major *et al.*, "P3HT as a pinhole blocking back contact for CdTe thin film solar cells," *Sol. Energy Mater. Sol. Cells*, vol. 172, pp. 1–10, Dec. 2017.
[14] O. S. Hutter, L. J. Phillips, K. Durose, and J. D. Major, "6.6% efficient antimony selenide solar cells using grain structure control and an organic contact layer," *Sol. Energy Mater. Sol. Cells*, vol. 188, pp. 177–181, Dec. 2018.
[15] B. Chen, M. Yang, S. J. Priya, and K. Zhu, "Origin of J–V hysteresis in perovskite solar cells," *J. Phys. Chem. Lett.*, vol. 7, no. 5, pp. 905–917, Feb. 2016.
[16] E. L. Unger *et al.*, "Hysteresis and transient behavior in current-voltage measurements of hybrid-perovskite absorber solar cells," *Energy Environ. Sci.*, vol. 7, no. 11, pp. 3690–3698, Oct. 2014.
[17] P. Blood and J. W. Orton, *The Electrical Characterization of Semiconductors: Majority Carriers and Electron States*. Cambridge, MA, USA: Academic Press, 1992.
[18] A. Walsh, D. O. Scanlon, S. Chen, X. G. Gong, and S. H. Wei, "Self-regulation mechanism for charged point defects in hybrid halide perovskites," *Angewandte Chemie—Int. Ed.*, vol. 54, no. 6, pp. 1791–1794, Feb. 2015.
[19] N. K. Elumalai, M. A. Mahmud, D. Wang, and A. Uddin, "Perovskite solar cells: Progress and advancements," *Energies*, vol. 9, no. 11, pp. 861–881, Oct. 25, 2016.
[20] Y. M. Haddara, P. Ashburn, and D. M. Bagnall, "Silicon–germanium: Properties, growth and applications," in *Springer Handbook of Electronic and Photonic Materials*. Cham, Switzerland: Springer, 2017.
[21] R. Schölin *et al.*, "Energy level shifts in spiro-OMeTAD molecular thin films when adding Li-TFSI," *J. Phys. Chem. C*, vol. 116, no. 50, pp. 26300–26305, Dec. 2012.
[22] J.-J. Shi *et al.*, "S-shaped current-voltage characteristics in perovskite solar cell," *Acta Physica Sinica*, vol. 64, no. 3, 2015, Art. no. 038402.
[23] W. Tress *et al.*, "Imbalanced mobilities causing S-shaped IV curves in planar heterojunction organic solar cells," *Appl. Phys. Lett.*, vol. 98, no. 6, pp. 063301–063303, 2011.